Advances in Science and Technology Research Journal

Advances in Science and Technology Research Journal, 2026, 20(8), 84–99
https://doi.org/10.12913/22998624/220620
ISSN 2299-8624, License CC-BY 4.0

Received: 2026.03.13
Accepted: 2026.06.01
Published: 2026.07.01

Experimental study on the influence of loading rate on the mechanical properties and microcrack evolution of sandstone under triaxial stress

Guozhu Wang[1,2], Wenchang Zhang[1,2*], Jian Li[1,2], Dongdong Wang[1,2], Hongjian Wang[3], Hao Zeng[1,2], Guiliang Li[1,2], Xitao Bao[1,2], Shuaizhi Ji[4], Hao Shi[5]

[1] Petroleum Engineering Institute, Zhongyuan Oilfield Company, SINOPEC, Puyang 457000, China
[2] SINOPEC Key Laboratory of Development Technology of Sour Natural Gas Fields, Dazhou 636150, China
[4] North China University of Water Resources and Electric Power, Zhengzhou 450046, China
[3] Technical Monitoring Center of Sinopec Zhongyuan Oilfield Branch,Puyang 457001, China
[5] School of Civil Engineering and Architecture, Anhui University of Science and Technology, Huainan, Anhui 232001, China
* Corresponding author's e-mail: 13623936139@163.com

ABSTRACT

To explore the coupled impacts of loading rate and confining pressure on the deformation, strength, and microcracking mechanisms of sandstone, triaxial compression tests were carried out under four distinct loading rates (0.001, 0.01, 0.1, and 1.0 mm/s) and four confining pressures (0, 20, 40, and 60 MPa), with concurrent monitoring of acoustic emission (AE). Leveraging moment tensor theory, the source mechanisms and microcrack propagation patterns of AE events were inverted. The findings reveal that as the loading rate rises, the peak strength increases from 27.18 MPa to 34.32 MPa under uniaxial compression and from 143.69 MPa to 164.34 MPa under a confining pressure of 60 MPa. Concurrently, the elastic modulus increases from 9.03 GPa to 10.88 GPa and from 16.74 GPa to 18.02 GPa, respectively, showing a positive linear relationship with the logarithmic loading rate. The peak strain is insensitive to loading rate under low-to-medium confining pressures but decreases by 18.42% under 60 MPa when the loading rate increases from 0.001 mm/s to 1.0 mm/s, revealing an inhibitory effect of high confining pressure combined with high loading rate on plastic deformation. Macroscopically, the failure mode transitions from brittle tensile splitting to ductile shearing as confining pressure increases. Analysis of AE source mechanisms indicates that shear cracks are predominant, constituting 55.3–72.4% of all events, with their proportion rising with loading rate. The total number of microcracks declines with increasing loading rate, from 1145 to 698 at a confining pressure of 20 MPa, suggesting that rapid loading inhibits full crack propagation. The AE *b*-value, which describes the slope of the frequency-magnitude distribution of AE events, decreases from 1.99 to 1.82 under 20 MPa confining pressure and from 1.89 to 1.68 under 60 MPa confining pressure as the loading rate increases, indicating a higher proportion of large-scale cracks and a more simplified crack network under rapid loading. This study deepens the comprehension of excavation rate effects in deep rock masses and provides a theoretical foundation for engineering stability assessment and disaster early warning.

Keywords: acoustic emission, loading rate, microcracking mechanism, moment tensor inversion, sandstone.

INTRODUCTION

In deep underground resource development and engineering construction, surrounding rock is subjected to complex high-stress environments over extended periods [1]. Excavation activities, as intense dynamic disturbances, significantly influence the stress adjustment, deformation response, and failure modes of surrounding rock through their advancement rates [2, 3]. Excessively rapid construction subjects the rock to extremely high stress loading rates [4, 5], inducing

transient strong disturbances that disrupt the original mechanical equilibrium and trigger brittle fracture instability. These disturbances manifest as macroscopic splitting, localized spalling, structural collapse, and high-energy rockbursts – all major engineering geological hazards [6]. The mechanical behavior of rock materials is also influenced by their compositional and microstructural characteristics, which can be modified by the presence of pores or additives [7–9]. Therefore, systematically investigating the strength, deformation, and fracture mechanisms of deep rock masses under varying loading rates is essential. It not only elucidates rock mechanical behavior under high-stress conditions but also provides a theoretical foundation for ensuring deep engineering safety, disaster prediction, and mitigation.

In recent years, extensive research has been conducted on the influence of loading rate on rock mechanical behavior, providing important references for deep rock engineering design and construction [10–15]. Mahmutoglu [16] performed dynamic uniaxial compression tests on marble and revealed that uniaxial compressive strength decreases significantly with decreasing loading rate. Li et al. [13] found that for hard rock, elastic modulus and Poisson's ratio are insensitive to strain rate changes within moderate ranges. Hashiba et al. [3] further examined the combined effects of water saturation and loading rate on andesite strength, highlighting the complexity of coupled environmental and dynamic factors. Although uniaxial tests generally show that compressive strength and elastic modulus increase with loading rate, the magnitude of this effect varies with lithology, mineral composition, and microstructure [17–19]. For instance, the elastic modulus of coarse-grained marble exhibits a nonlinear response to loading rate, first decreasing and then increasing [20], whereas coal shows an initial increase followed by a decrease [21]. However, uniaxial conditions cannot accurately represent the triaxial stress state of deep surrounding rock. Consequently, research has increasingly shifted toward triaxial compression conditions [22, 23]. A series of triaxial tests have demonstrated that confining pressure significantly alters rock failure modes and strength characteristics. Under high confining pressure, rocks transition from brittle to ductile behavior, and their loading rate sensitivity also changes significantly [24–27]. However, existing research has primarily focused on macroscopic mechanical parameters, with limited investigation into the evolution of microcracks under confining pressure. In particular, the microcracking mechanisms of deep sandstone under triaxial stress states require further exploration.

Acoustic emission (AE) technology, a real-time, high-precision method for monitoring microcracks, captures elastic waves released during internal rock damage, providing crucial data for studying the spatiotemporal evolution of crack processes [28–31]. This technology has been widely applied in rock mechanics research [32–34]. Sun et al. analyzed AE parameter evolution during deformation in marble and granite under uniaxial compression at different loading rates, achieving pre-failure identification based on AE signals. Cao et al. [36] systematically investigated the effects of loading rate on mechanical properties, AE parameters, and damage evolution in sandstone. Feng et al. [37] conducted uniaxial compression AE tests on sandstone at varying loading rates, analyzing the distribution characteristics of AE events and performing scanning electron microscopy on fragments from regions with and without AE activity. This enabled investigation of loading rate effects on AE event formation mechanisms at the microscale. These studies deepen our understanding of loading rate effects on AE behavior. However, existing work primarily focuses on statistical analysis of AE parameters (e.g., ringing counts, energy release rates, event rates), with limited exploration of the underlying physical mechanisms and crack evolution patterns. Specifically, AE events originate from diverse microcrack activities (tension, shear, compression, and mixed modes). Their proportions and spatiotemporal evolution directly reflect internal damage accumulation and macroscopic failure progression. Yet the generation mechanisms of these multi-type crack sources under varying loading rates remain unclear.

Given the current research status and practical demands of deep engineering, this study conducts acoustic emission monitoring experiments on deep sandstone under triaxial stress conditions with varying loading rates. Through systematic analysis of loading rate effects on sandstone strength, deformation, and AE behavior, combined with AE localization and moment tensor inversion, we investigate the generation mechanisms, typological evolution, and spatiotemporal clustering characteristics of microcrack sources during different deformation stages. The aim is to reveal the loading rate effect mechanisms governing damage

accumulation and crack evolution in sandstone under high-stress environments, providing a theoretical foundation and experimental support for evaluating rock mass stability and predicting dynamic hazards in deep engineering.

EXPERIMENTAL SCHEME

Specimen preparation

The sandstone specimens were taken from an ultra-low permeability reservoir in the Dongying Depression, Bohai Bay Basin, eastern China. This reservoir is representative of typical deep tight sandstones widely distributed in continental rift basins, characterized by low porosity (9–12%), low permeability (0.1–1 mD), and complex pore structures. The sandstone specimens were prepared from a single large block to ensure homogeneity. All specimens were machined into standard cylinders (50 mm diameter × 100 mm height) in accordance with the International Society for Rock Mechanics (ISRM) recommendations (Figure 1). The machining tolerances were strictly controlled, with end surface flatness within 0.02 mm and perpendicularity to the axis within 0.001 rad. To avoid moisture effects, the specimens were stored in a sealed, constant-temperature container prior to testing. The average natural moisture content, density, and longitudinal wave velocity were 2.0%, 2302 kg/m^3, and 2490 m/s, respectively, indicating a uniform texture and dense structure.

Fresh fracture surfaces of the specimens were examined using a ZEISS scanning electron microscope (SEM). The SEM images (Figure 2) reveal that the pore structure is dominated by intergranular pores, which form a network-like distribution with good connectivity. In addition, mixed-layer illite/smectite clay minerals are developed within the pores and on grain surfaces. This microstructure plays a significant role in the mechanical behavior: the well-connected pore network facilitates stress concentration and crack propagation, while the presence of clay minerals may promote microcrack nucleation and affect the shear/tensile crack ratio under different loading rates.

It should be noted that sandstones from different geological settings (e.g., quartz-rich arenites, carbonate-cemented sandstones) may exhibit different mineral compositions, cementation types, and pore structures, which can influence their loading rate sensitivity. Therefore, the conclusions drawn from this specific sandstone are primarily applicable to similar tight sandstones in continental rift basins; extrapolation to other sandstone types requires further validation.

Test system

The test system used in this study consists of a TAW-2000 electro-hydraulic servo rock mechanics testing system, a DS5-16B acoustic emission (AE) system, and a load–deformation acquisition system. The TAW-2000 system is capable of applying a maximum axial load of 3000 kN and a maximum confining pressure of 140 MPa, enabling conventional triaxial, creep, relaxation, and other types of tests. In this experiment, eight AE sensors were used. To prevent the sensors from falling off during specimen failure, which could lead to incomplete data acquisition, they were secured with adhesive tape at a distance of 10 mm from the ends of the specimen. The AE acquisition system was set with a threshold of 40 dB, a time interval of 40 μs, and a sampling frequency of 1 MHz. The test system is illustrated in Figure 3.

Loading scheme

Preliminary test results showed that the uniaxial compressive strength of the sandstone

Figure 1. Prepared sandstone specimens

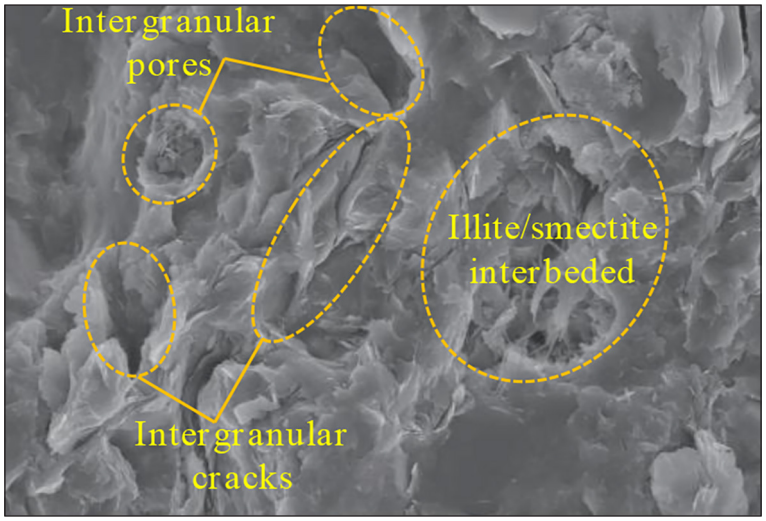

Figure 2. Scanning electron microscope images of experimental samples

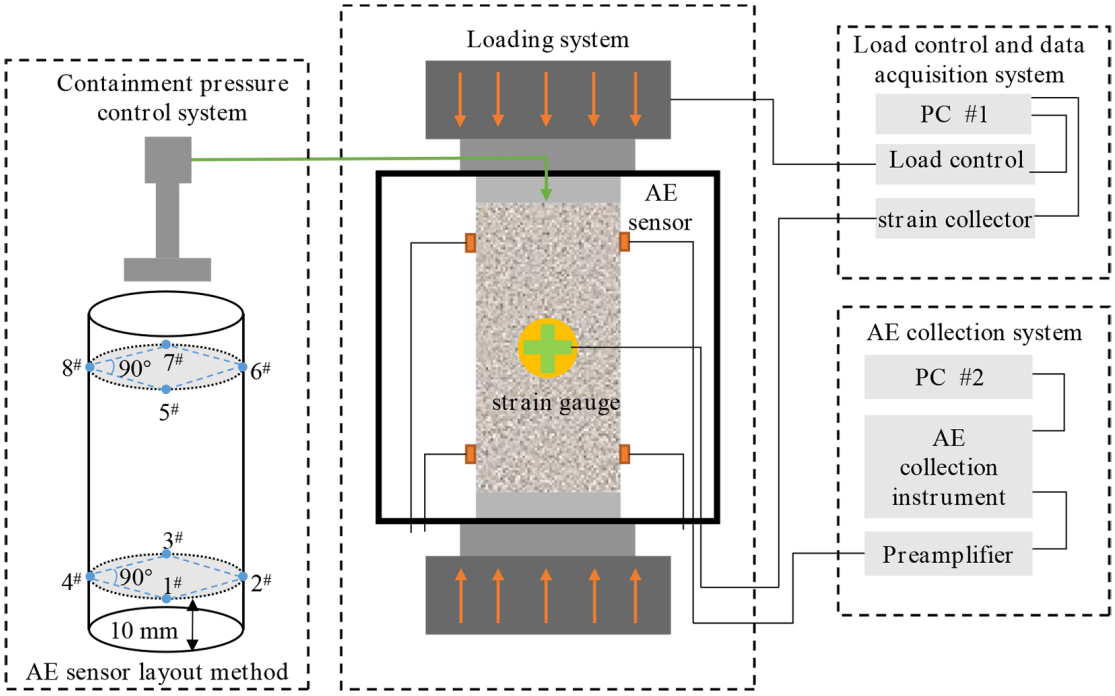

Figure 3. Test system

specimens is approximately 32 MPa. When the confining pressure reaches 60 MPa, the specimens exhibit ductile behavior, and the stress–strain curve approaches ideal elastoplasticity. Based on practical engineering conditions, the strain rates induced by tunnel excavation are generally within the quasi-static range; for example, they do not exceed 10^{-1} s^{-1} in coal mining [38]. Generally, strain rates ranging from 10^{-5} to 10^{-2} s^{-1} are considered quasi-static [39]. Based on the height of the sandstone specimens, the displacement loading rates of the testing machine were set to 0.001, 0.01, 0.1, and 1.0 mm/s. Therefore, constant loading rate tests were conducted under four different confining pressures (0, 20, 40, and 60 MPa) and four different loading rates (0.001, 0.01, 0.1, and 1.0 mm/s). To minimize the effects of variability, three parallel tests were conducted for each condition.

AE localization and moment tensor theory

This study employs the autoregressive model and Akaike's Information Criterion (AIC) to

identify signal arrival times [40], and uses the simplex method for AE event localization [41].

Moment tensor inversion aims to infer source characteristics from recorded surface displacements. The moment tensor itself is a symmetric 3 × 3 tensor containing couples and moments that fully describe the source mechanism. Pujol and Herrmann [42] formulated this problem as:

$$u_k = G_{ki,j} M_{ij} \tag{1}$$

where: u_k is the displacement field recorded by sensor k; $G_{ki,j}$ is the linear Green's function for wave propagation between the source and the sensor.

According to the decomposition method of Knopoff and Randall [43], the moment tensor is decomposed into three components: the isotropic (ISO), compensated linear vector dipole (CLVD), and double-couple (DC) components.

$$\begin{aligned} M &= M_{\mathrm{ISO}} + M_{\mathrm{CLVD}} + M_{\mathrm{DC}} = \\ &= \tfrac{1}{3} tr(M) \begin{pmatrix} 1 & 0 & 0 \\ 0 & 1 & 0 \\ 0 & 0 & 1 \end{pmatrix} + |\varepsilon| m^*_{max} \begin{pmatrix} -1 & 0 & 0 \\ 0 & -1 & 0 \\ 0 & 0 & 2 \end{pmatrix} + \\ &+ (1 - 2|\varepsilon|) m^*_{max} \begin{pmatrix} -1 & 0 & 0 \\ 0 & 0 & 0 \\ 0 & 0 & 1 \end{pmatrix} \end{aligned} \tag{2}$$

where: $\varepsilon = -m^*_{min}/|m^*_{max}|$, m^*_{min} and m^*_{max} are the absolute minimum and maximum eigenvalues of the deviatoric tensor, respectively, and $tr(M)$ is the trace of the moment tensor (i.e., the sum of its eigenvalues).

For each AE event, the moment tensor corresponding to the maximum scalar moment is retained. The scalar moment M_0 is given by:

$$M_0 = \sqrt{\frac{1}{2} \sum_{i,j=1}^{3} m_{ij}^2} \tag{3}$$

The Richter magnitude M can then be calculated from M_0 as :

$$M = \frac{2}{3} \lg(M_0) - 6 \tag{4}$$

In seismology, the b-value, which characterizes the slope of the frequency-magnitude distribution, is a widely used parameter for assessing the crack state of a region. This relationship was first established by Gutenberg and Richter [44], who demonstrated that earthquake frequency decreases exponentially with magnitude, a law now known as the Gutenberg-Richter (G-R) relation:

$$\mathrm{Log} N = a - bM \tag{5}$$

where: M is the Richter magnitude (proportional to the logarithm of the maximum amplitude recorded), N is the number of earthquakes of that magnitude, a is an empirical constant, and b is the b-value.

The b-value describes the magnitude distribution: a larger b-value reflects a higher proportion of small-magnitude events, whereas a smaller b-value reflects a higher proportion of large-magnitude events.

Based on moment tensor decomposition, the crack type of AE events is determined using the criteria of Feigner and Young [45]:

$$R = \frac{tr(M) \times 100}{|tr(M)| + \sum_{k=1}^{3} |m_k^*|} \tag{6}$$

where: m^*_k are the eigenvalues of the deviatoric moment tensor, and tr(M) is the trace (sum of eigenvalues), which represents the volume change at the AE source.

The crack type is then classified based on the parameter R as follows: R>30% indicates tensile failure; −30%≤R≤30% indicates shear failure; R<−30% indicates compressive failure.

Hudson et al. [46] proposed another analysis method using two parameters, T and k. Let M_1>M_2>M_3 be the three principal eigenvalues of the moment tensor. Then the T and k values can be expressed as:

$$T = \frac{2m_2^*}{\max\left(|m_1^*, m_3^*|\right)} \tag{7}$$

$$k = \frac{tr(M)/3}{|tr(M)/3| + \max\left(|m_1^*, m_3^*|\right)} \tag{8}$$

where: T measures the deviatoric component (−1 for pure positive CLVD, +1 for pure negative CLVD, 0 for pure double-couple), and k measures the isotropic component (+1 for pure explosion, −1 for pure implosion).

These parameters are plotted on the Hudson diagram shown in Figure 4.

TEST RESULTS

Strength and deformation characteristics

Based on triaxial compression tests on sandstone conducted under various loading rates (v) and confining pressures (σ_3), the following mechanical parameters were systematically analyzed: the peak deviatoric stress ($\sigma_p=\sigma_{1max}-\sigma_3$), the elastic modulus ($E$, defined as the slope of the linear portion of the stress-strain curve), and the peak strain (ε_p, the axial strain at peak strength). For each combination of loading rate and confining pressure, three specimens were tested. The values presented in Table 1 are mean values of the three repeated tests.

Figure 5 show the mean values and their variability (error bars in Figure 5 represent standard deviation). Table 1 and Figure 5(a) show that the peak deviatoric stress σ_p depends strongly on both confining pressure and loading rate. At any given loading rate, σ_p increases significantly with increasing confining pressure σ_3. For example, at a loading rate of 0.01 mm/s, increasing the confining pressure from 0 MPa to 60 MPa raises σ_p from 29.77 MPa to 152.12 MPa, corresponding to a 410.98% increase. This demonstrates the strengthening effect of confining pressure, which enhances the rock's bearing capacity by inhibiting microcrack propagation and promoting frictional interlocking between mineral particles.

In addition, under a fixed confining pressure, σ_p increases with loading rate v and exhibits a strong linear positive correlation with $\log_{10}(v)$. Linear fitting results are presented in Table 2 (based on the mean values from Table 1), with all correlation coefficients $R^2>0.967$, indicating a highly significant relationship. The slope a of the fitted line represents the rate sensitivity of strength. As shown in the Table 2, a increases monotonically with confining pressure, from 2.466 under uniaxial conditions to 6.582 at 60 MPa. This trend quantitatively indicates that confining pressure not only increases rock strength but also enhances its sensitivity to loading rate. In other words, in deep high-stress environments, minor changes in loading rate can induce more pronounced strength variations compared to shallow low-stress conditions.

The elastic modulus E also exhibits a clear dependence on confining pressure and loading rate. Table 1 and Figure 5(b) show that E increases with σ_3, primarily because confining pressure closes internal microcracks, enhancing the stiffness of the rock skeleton. Under constant confining pressure, E also increases with loading rate v. For example, at σ_3=20 MPa, increasing v from 0.001 to 1.0 mm/s raises E from 11.01 to 12.98 GPa, corresponding to an increase of approximately 17.89%. However, compared with the peak strength, the rate of increase in E is generally lower, indicating that loading rate has a weaker effect on rock stiffness than on strength.

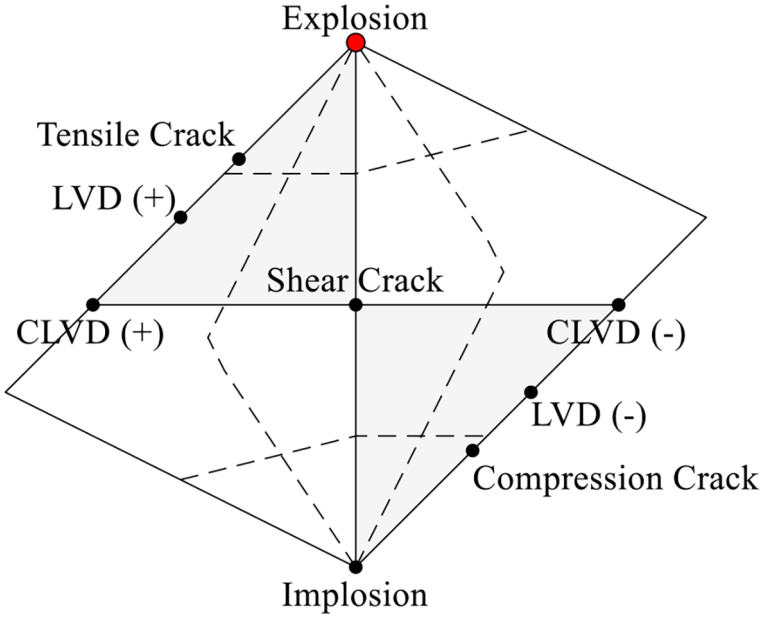

Figure 4. Hudson source type plot

Table 1. Mechanical parameters of sandstone samples under different confining pressures and loading rates

Loading rate /mm/s	σ_3/MPa	Average value		
		σ_p/MPa	E/GPa	ε_p/%
0.001	0	27.18	9.03	0.37
	20	93.24	11.01	1.05
	40	121.04	14.02	1.39
	60	143.69	16.74	2.28
0.01	0	29.77	9.86	0.42
	20	98.38	11.55	1.15
	40	124.92	14.97	1.44
	60	152.12	17.01	2.22
0.1	0	33.01	10.18	0.45
	20	100.97	12.26	1.19
	40	129.45	15.19	1.57
	60	155.99	17.28	2.01
1.0	0	34.32	10.88	0.47
	20	103.56	12.98	1.23
	40	136.86	15.72	1.55
	60	164.34	18.02	1.86

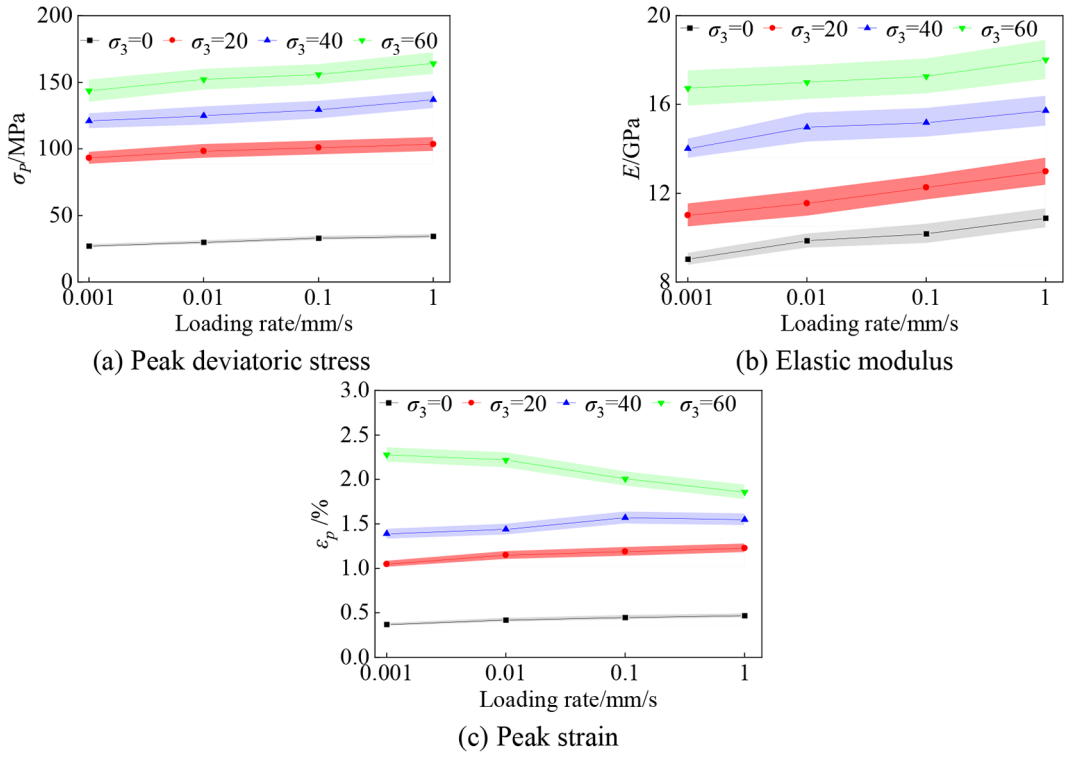

Figure 5. Strength and deformation parameters of sandstone specimens under different confining pressures and loading rates

In contrast, the peak strain ε_p exhibits a more complex response, with a rate sensitivity that depends on confining pressure (Figure 5c). Under low to medium confining pressures (0–40 MPa), ε_p either increases slightly with $\log_{10}(v)$ or remains relatively stable. For instance, at σ_3=20 MPa, ε_p increases from 0.0105 at v=0.001 mm/s to 0.0123 at v=1.0 mm/s. Under high confining pressure (60 MPa), however, ε_p shows a pronounced negative rate sensitivity: as v increases

Table 2. Linear fitting parameters between peak strength σ_p of sandstone and logarithm of loading rate $\log_{10}(v)$

σ_3 /MPa	Fitting formula $\sigma_p = a \times \log_{10}(v) + b$	R^2	a
0	$\sigma_p = 2.466 \times \log_{10}(v) + 34.76$	0.976	2.466
20	$\sigma_p = 3.355 \times \log_{10}(v) + 104.07$	0.967	3.355
40	$\sigma_p = 5.199 \times \log_{10}(v) + 135.866$	0.976	5.199
60	$\sigma_p = 6.582 \times \log_{10}(v) + 163.908$	0.981	6.582

from 0.001 to 1.0 mm/s, ε_p decreases from 0.0228 to 0.0186, a reduction of 18.42%. This behavior has important implications for the deformation mechanism. Under high confining pressure, the rock approaches a brittle–ductile transition, but a high loading rate suppresses the time-dependent microscopic processes required for ductile deformation (e.g., grain boundary sliding, stable microcrack propagation, and particle rearrangement). Consequently, the rock reaches its bearing capacity with less accumulated plastic strain and enters the instability failure stage earlier. These observations highlight the inhibitory effect of high confining pressure combined with high loading rate on the plastic deformation capacity of rock.

Transition of macroscopic failure modes

In addition to affecting the strength and deformation parameters of sandstone, the combined effects of loading rate and confining pressure also profoundly modify its macroscopic failure mode. Figure 6 illustrates the stress–strain curves and representative failure morphologies of sandstone under various confining pressures, exemplified by a loading rate of 0.01 mm/s.

Under uniaxial compression (σ_3=0 MPa), the stress–strain curve exhibits typical brittle behavior. The linear elastic segment has a stable slope, and upon reaching peak strength, the stress drops abruptly. The specimen splits into multiple longitudinal fragments, with failure surfaces consisting mainly of tensile cracks parallel to the loading direction. No visible shear marks are observed, indicating a typical tensile splitting failure.

When the confining pressure increases to 20 MPa, the curve exhibits a clear yield plateau near the peak. The post-peak stress drop becomes gradual, and the residual strength increases significantly. After failure, the specimen exhibits a single through-going shear plane, with white powdery wear debris visible on the surface – evidence of frictional sliding. This indicates a transition from tensile to shear-dominated failure, characteristic of single-plane shear failure.

At a confining pressure of 60 MPa, the stress–strain curve approaches ideal elastic–plastic behavior, and some specimens even exhibit slight strain hardening. Upon failure, no distinct macroscopic fracture plane is observed; instead, the specimen undergoes uniform bulging deformation, with dense intersecting micro-shear band networks on the lateral surface. The rock enters the ductile failure regime. This transition in failure modes clearly demonstrates the inhibitory effect of confining pressure on tensile cracking and its promoting effect on shear sliding.

Acoustic emission characteristics and microcracking evolution

Spatiotemporal evolution of AE events and spatial distribution of crack ypes

The spatiotemporal distribution of AE events directly reveals the initiation, propagation, and clustering of internal damage in rocks. Figure 7 shows the localization results of AE events during typical pre-peak stress stages, using specimens tested at a loading rate of 0.01 mm/s under different confining pressures as examples. In the figure, different colors represent crack types identified by the *R*-value method [45] (blue: tensile; red: shear; cyan: compressive), and sphere size corresponds to event magnitude.

In all specimens, tensile and shear cracks are the dominant types, while compressive cracks are rare (Figure 7). This indicates that even under uniaxial compression, the microscopic failure process is not purely tensile; a significant number of shear microcracks also develop. Under uniaxial conditions (Figure 7a), AE events are relatively dispersed, with a high proportion of tensile cracks. As the confining pressure increases to 20 MPa (Figure 7b), AE events begin to cluster along the direction of the future macroscopic shear zone, and the proportion of shear cracks increases significantly. At 60 MPa (Figure 7c), the AE events become more

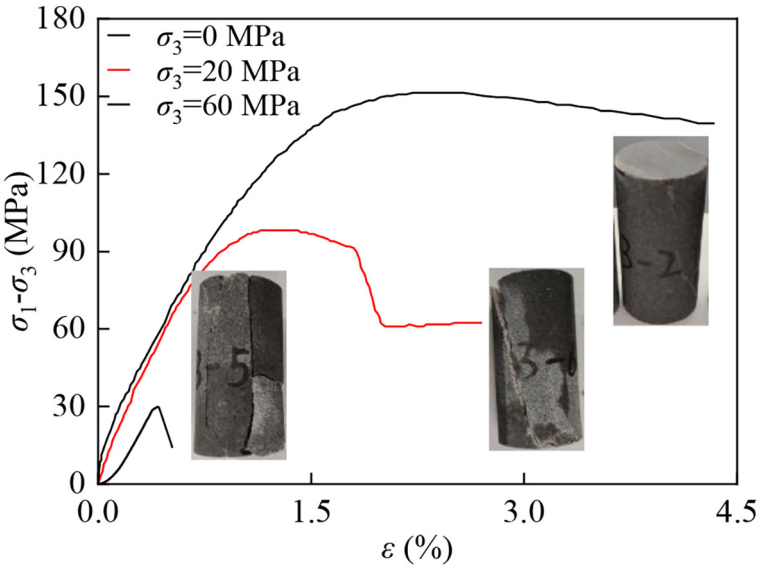

Figure 6. Typical stress-strain curves and macroscopic failure modes (v=0.01 mm/s)

diffuse, no longer confined to a single shear zone, instead forming multiple interwoven microcrack clusters. This corresponds well to the macroscopic transition to ductile failure and the development of multiple micro-shear band networks under high confining pressure. At this stage, the proportion of shear cracks continues to increase while tensile cracks further decrease, indicating that under high confining pressure, internal damage is dominated by shear mechanisms, and the crack distribution becomes more uniform.

To quantitatively analyze the proportions of microcrack types, all AE events under different test conditions were classified using the *R*-value method. The results are listed in Table 3. Under all test conditions, shear cracks dominate, accounting for 55.3% to 72.4% of the total events. As confining pressure increases, the proportion of shear cracks rises significantly, while that of tensile cracks decreases correspondingly. For instance, at a loading rate of 0.001 mm/s, an increase in confining pressure from 0 to 60 MPa raises the shear crack proportion from 55.3% to 69.9%, while the tensile crack proportion drops from 38.2% to 26.9%. Compressive cracks account for a small proportion (2.8–6.5%) and generally decrease with increasing confining pressure, with slight variations depending on loading rate.

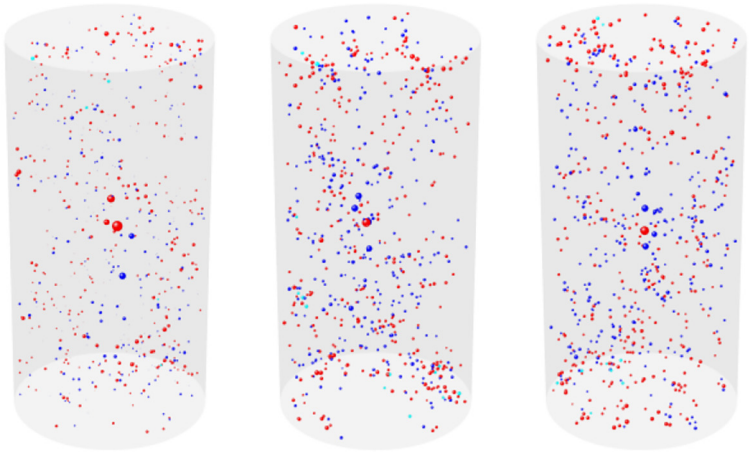

(a) σ_3 = 0 MPa (b) σ_3 = 20 MPa (c) σ_3 = 60 MPa

Figure 7. Spatial distribution of pre-peak AE events in sandstone under different confining pressures (v=0.01 mm/s)

Table 3. Statistics of microcrack types under different testing conditions

Loading rate/mm/s	σ_3/MPa	Total events	Tensile/%	Shear/%	Compressive/%
0.001	0	1023	38.2	55.3	6.5
	20	1145	34.1	61.2	4.7
	40	1256	30.5	65.8	3.7
	60	1342	26.9	69.9	3.2
0.01	0	886	37.5	56.0	6.5
	20	972	33.8	61.5	4.7
	40	1068	29.7	66.3	4.0
	60	1154	26.2	70.8	3.0
0.1	0	752	36.9	56.8	6.3
	20	826	33.0	62.4	4.6
	40	905	29.1	67.2	3.7
	60	989	25.5	71.6	2.9
1	0	635	35.8	58.0	6.2
	20	698	32.2	63.3	4.5
	40	767	28.4	68.0	3.6
	60	843	24.8	72.4	2.8

Under a given confining pressure, the total number of events decreases markedly with increasing loading rate (e.g., at σ_3= 20 MPa, from 1145 at 0.001 mm/s to 698 at 1.0 mm/s). At high loading rates, faster crack propagation leaves insufficient time for new cracks to initiate over a wider area, resulting in fewer total events and more localized fracturing along the main fracture zone. This indicates that rapid loading inhibits the full initiation and propagation of microcracks. Concurrently, the proportion of shear cracks increases slightly under high loading rates, while that of tensile cracks decreases slightly, suggesting that rapid loading tends to promote shear microcracks.

Focal mechanism analysis based on Hudson plot

Figure 8 illustrates the focal mechanisms of AE events for specimens tested at a confining pressure of 20 MPa under different loading rates. All identified AE events are projected onto the Hudson source type plot, where each point represents an event, with its position defined by the T and k values.

In Figure 8, AE events are approximately distributed along the diagonal between tensile and compressive failure. The events are neither purely tensile cracks nor ideal shear (double-couple) or pure compression types. All cracks exhibit significant mixed-mode characteristics. Tensile events contain a notable shear (deviatoric) component; shear events are mixed with volumetric (isotropic) components, indicating either dilation or compression; compressive events are accompanied by a significant shear component.

Comparison of Figures 8(a)–(d) shows that the distribution range of AE event points changes with increasing loading rate. At low loading rates (Figure 8a), the points are more dispersed, covering a wider range from compression to dilation, indicating greater diversity in crack types. At high loading rates (Figure 8d), the point distribution contracts toward T=0 (shear) and k=0, indicating that the crack mechanism becomes simpler and more shear-dominated.

This phenomenon provides focal mechanism evidence that high loading rates inhibit the full development of tensile and compressive microcracks, thereby promoting a shear-dominated crack mode. This not only reveals the influence of loading rate on the microcrack mechanism of rock but also provides microscale evidence for understanding rock failure behavior under different strain rate conditions.

b-value analysis

Figure 9 shows the magnitude frequency distribution of AE events for sandstone specimens tested at σ_3=20 MPa under different loading rates. The b-value serves as a key parameter reflecting the stress state and crack scale distribution within the medium. The moment magnitudes and frequencies of AE events under various conditions

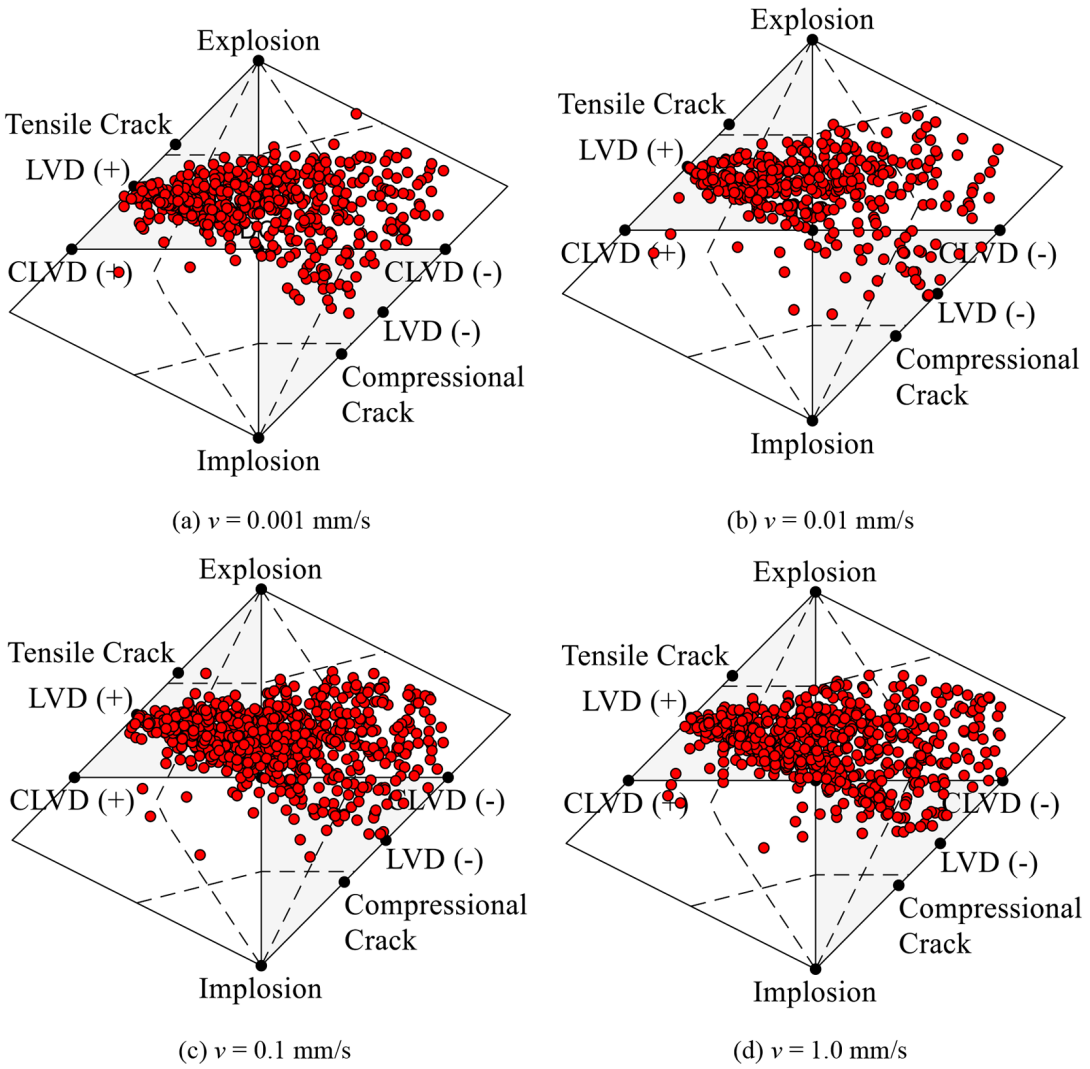

Figure 8. Hudson source type plots for sandstone AE events under different loading rates (σ_3=20 MPa)

were analyzed, and the *b*-values were fitted using the Gutenberg–Richter (G–R) formula. The results are presented in Table 4.

Under a given confining pressure, the *b*-value decreases significantly with increasing loading rate. For instance, at 20 MPa, as the loading rate increases from 0.001 mm/s to 1.0 mm/s, the *b*-value drops from 1.99 to 1.82, a decrease of approximately 8.5%. At 60 MPa, the *b*-value decreases from 1.89 to 1.68, a reduction of about 11.1%. A lower *b*-value indicates an increased proportion of large-scale crack events and a reduced proportion of small-scale events, suggesting that high loading rates accelerate crack propagation and promote larger-scale cracking.

At a given loading rate, the *b*-value also decreases with increasing confining pressure. For example, at 0.001 mm/s, increasing the confining pressure from 0 to 60 MPa reduces the *b*-value from 2.11 to 1.89, a decrease of approximately 10.4%. This indicates that high confining pressure similarly promotes large-scale cracking, consistent with the macroscopic transition to ductile behavior and the formation of more concentrated shear zones under high confining pressure. The effects of loading rate and confining pressure on the *b*-value are cumulative. The highest *b*-value (2.11) occurs under low loading rate and low confining pressure, while the lowest (1.68) appears under high loading rate and high confining pressure. This further demonstrates that both factors increase crack scale, with their combined effect being more pronounced.

At low loading rates, cracks propagate slowly, allowing ample time for numerous microcrack nucleation events and the formation of complex crack networks. Consequently, small events dominate, yielding a high *b*-value. At high loading rates, rapid stress concentration and high energy input

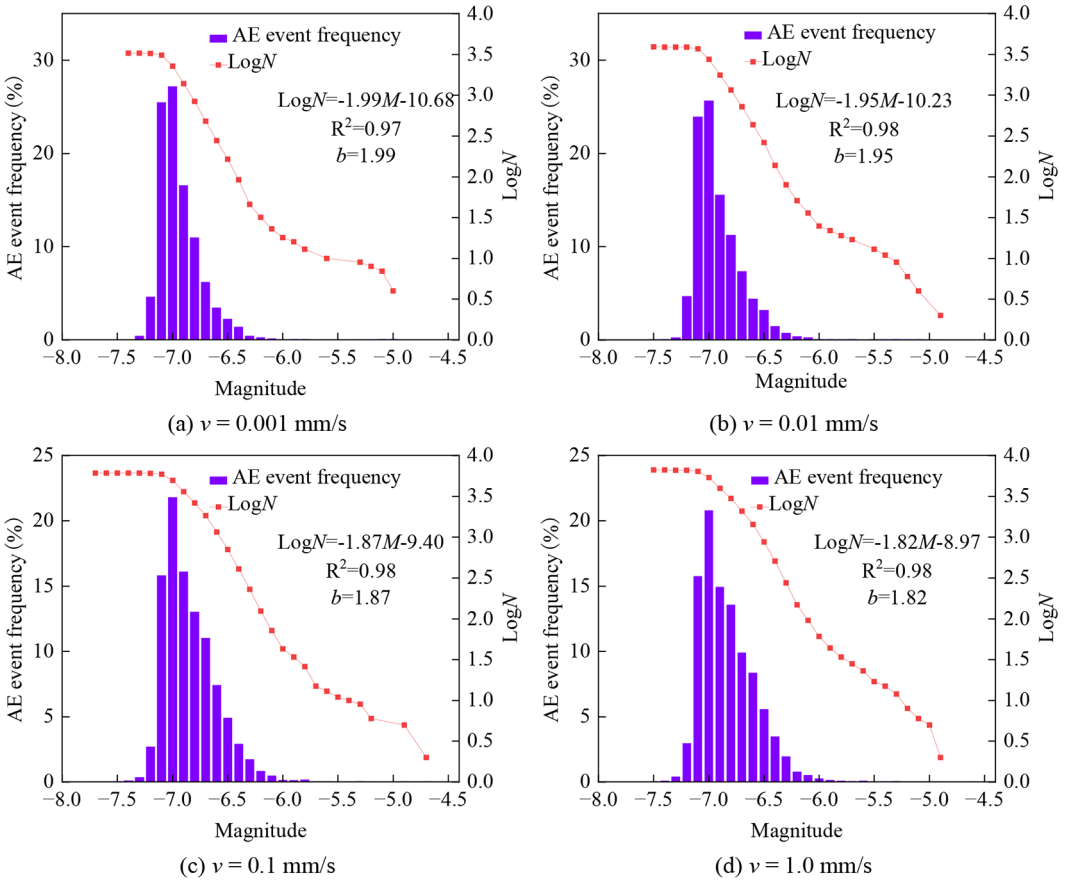

Figure 9. Distribution and *b*-value fitting of acoustic emission magnitude frequency at different loading rates (σ_3=20 MPa)

Table 4. *B*-values under different loading rates and confining pressures

Loading rate (mm/s)	σ_3=0	σ_3=20	σ_3=40	σ_3=60
0.001	2.11	1.99	1.90	1.89
0.01	2.03	1.95	1.85	1.82
0.1	1.95	1.87	1.80	1.75
1	1.88	1.82	1.72	1.68

rates inhibit crack branching and dispersion. Cracks propagate unstably and coalesce quickly, forming large-scale crack sources. This results in simplified, concentrated crack networks and a low *b*-value.

At low confining pressures, cracks tend to propagate as tensile cracks, generating numerous small-scale cracks. At high confining pressures, cracks propagate primarily in a shear-dominated manner, more readily forming localized through-going large-scale cracks. According to Turcotte [47], the spatial fractal dimension D of the crack network is approximately equal to 2*b*. Thus, the *b*-value also reflects the complexity of the crack network. In this study, the decrease in *b*-value with increasing loading rate and confining pressure quantitatively demonstrates that crack networks formed under these conditions are simpler and more concentrated. This provides a theoretical basis for using microseismic *b*-values to monitor and predict rock mass stability at the engineering scale.

DISCUSSION

Investigation of the micro-mechanism of the loading rate effect

This study systematically revealed the influence of loading rate on the mechanical behavior of sandstone, from macroscopic parameters and

failure modes to microcrack mechanisms. The essence of the loading rate effect lies in its control over the time dependence and energy distribution of internal damage evolution.

At low loading rates, the gradual increase in load allows ample time for stress redistribution within the rock. Stress concentration at crack tips is slowly released and adjusted through the development of plastic zones, stable microcrack propagation, and slip along grain boundaries. Consequently, numerous cracks form within a complex crack network (high *b*-value), leading to diverse failure modes. This ultimately enables the rock to accumulate significant plastic deformation before failure, exhibiting strong ductile characteristics.

At high loading rates, loads are applied rapidly, resulting in massive energy input over a short period. The rock lacks sufficient time for stress adjustment and energy dissipation, leading to a sharp increase in stress concentration. This has two consequences: First, the driving force for crack propagation becomes immense. Once initiation conditions are met, cracks propagate rapidly and may undergo abrupt coalescence, suppressing the nucleation and development of secondary cracks. Consequently, the total number of cracks is low, and the crack network is simple (low *b*-value). Second, rapid loading may force deformation that would normally require shear slip to occur through more direct, faster tensile or mixed failure. However, under high confining pressure, tensile failure is suppressed, leading to a higher proportion of shear failure. This shear-dominated failure involves a greater volumetric component, and the change in damage mechanism ultimately causes the rock to fail at a lower cumulative strain.

Engineering implications of high confining pressure-high loading rate coupling

The negative strain rate sensitivity of peak strain observed under high confining pressure has significant engineering implications. This finding is consistent with the field observations of Zhuang et al. [17], who reported that increasing the advance rate of a longwall face intensifies mining-induced stress concentrations and microseismic activity, thereby reducing the rock's capacity for ductile adjustment and promoting brittle failure. It indicates that rapid excavation in deep, high-stress environments prevents the full exploitation of rock mass plasticity, leading to enhanced brittle behavior. This implies that despite potentially high measured rock strength, the failure suddenness and energy release intensity will increase markedly. Therefore, relying solely on static parameters for deep engineering design may be hazardous; the influence of excavation rate must be fully considered. Appropriately controlling the excavation rate to allow time for stress adjustment and energy dissipation is an effective strategy to utilize the rock's plastic potential and avoid brittle dynamic failure. This strategy aligns with the recommendations of Hajiabdolmajid and Kaiser [14], who emphasized that controlled deformation and rate management are key to preventing brittle collapse in hard rock tunneling.

Furthermore, the variation pattern of the *b*-value provides important guidance for in-situ microseismic monitoring. In engineering practice, real-time monitoring of *b*-value changes can assess rock mass stability. A sustained decrease in the *b*-value indicates an increasing proportion of large-scale cracking events and approaching instability, necessitating timely warnings and adjustments to the excavation rate.

Research limitations and future prospects

Although this study has yielded valuable insights, certain limitations remain. First, the experiments only considered the conventional triaxial compression stress path ($\sigma_1>\sigma_2=\sigma_3$), whereas actual engineering scenarios involve complex and variable stress paths (e.g., unloading, true triaxial stress states). The effects of loading rates under these complex conditions require further investigation. Second, significant scale differences exist between laboratory-scale (centimeter-level) acoustic emission events and engineering-scale (meter to hundred-meter-level) microseismic events. Challenges remain in effectively applying the crack mechanisms and *b*-value patterns revealed in laboratory tests to the interpretation of engineering-scale microseismic monitoring.

Future work should establish micro-damage constitutive models that accurately describe loading rate effects and integrate them into numerical simulation software to achieve high-fidelity simulations of deep engineering rock mass responses. Concurrently, combining true triaxial tests, unloading tests, and advanced AE inversion techniques can deepen the investigation of loading rate effects under complex stress paths, providing more reliable theoretical support for deep engineering safety.

CONCLUSIONS

This study systematically investigated the effects of loading rate on the mechanical properties and microcrack evolution of sandstone through triaxial compression tests combined with acoustic emission monitoring and moment tensor inversion. The main findings are as follows:

Both peak strength and elastic modulus increase with loading rate, showing a significant positive linear correlation with the logarithm of loading rate. Higher confining pressure enhances the sensitivity of peak strength to loading rate. At a confining pressure of 60 MPa, as the loading rate increases from 0.001 mm/s to 1.0 mm/s, the peak strength increases from 143.69 MPa to 164.34 MPa, and the elastic modulus rises from 16.74 GPa to 18.02 GPa.

Under low to medium confining pressures, peak strain exhibits insensitivity or a positive correlation with loading rate; however, under high confining pressure (60 MPa), it shows a pronounced negative rate sensitivity, with peak strain decreasing from 2.28% to 1.86% as loading rate increases from 0.001 mm/s to 1.0 mm/s, indicating that high confining pressure coupled with high loading rate inhibits plastic deformation capacity. Macroscopic failure mode transitions from brittle tensile splitting to ductile shearing as confining pressure increases.

AE source mechanism analysis reveals that most crack events exhibit mixed-mode characteristics; pure tensile or pure shear events are rare, and shear mechanisms remain consistently dominant. The total number of microcracks decreases with increasing loading rate. At a confining pressure of 20 MPa, the total number decreases from 1145 events at 0.001 mm/s to 698 events at 1.0 mm/s. The *b*-value decreases with increasing loading rate, from 1.99 to 1.82 at 20 MPa confining pressure, and from 1.89 to 1.68 at 60 MPa confining pressure, indicating a higher proportion of large-scale cracks and a simpler, more concentrated crack network under high loading rates.

This study enhances the understanding of excavation rate effects in deep rock masses and offers a theoretical basis for engineering stability assessment and disaster early warning.

Acknowledgements

This research was supported by the Zhongyuan Oilfield Postdoctoral Fund (No. 2024BY03), the Sinopec Ten Dragon Science and Technology Research Project (No. P24231), the Sinopec Technology Research and Development Project (No. P25160), the Young Backbone Teachers of Undergraduate Universities in Henan Province (No. 2023GGJS077), the Key Research and Development Project of Henan Province (No. 241111321100), and the Open Fund of the National Key Laboratory of Intelligent Coal Mining and Rock Control (No. SKLIS202421).

REFERENCES

1. Li W, Guo Y, Liu X, et al. Failure mechanisms and reinforcement support of soft rock roadway in deep extra-thick coal seam: A case study[J]. Engineering Failure Analysis, 2024;165:108745.
2. Chen L, Lyu S, Guo Z, et al. Experimental investigation on effect of loading rate on fracture behavior of coal-seam roof rock[J]. Energy Exploration & Exploitation, 2023;41(5):1746–1761.
3. Hashiba K, Fukui K, Kataoka M. Effects of water saturation on the strength and loading-rate dependence of andesite[J]. International Journal of Rock Mechanics and Mining Sciences, 2019;117:142–149.
4. Li M, Lin Z, Shi S, et al. Experimental research on influence mechanism of loading rates on rock pressure stimulated currents[J]. International Journal of Mining Science and Technology, 2023;33(2):243–250.
5. Riabokon E, Turbakov M, Popov N, et al. Study of the influence of nonlinear dynamic loads on elastic modulus of carbonate reservoir rocks[J]. Energies, 2021;14(24):8559.
6. Rouhani H, Arash M, Farrokh E. Investigating the effects of confining pressure and loading rate on damage propagation and mode I stress intensity factor of granite using the RHT constitutive model[J]. Geomechanics and Geophysics for Geo-Energy and Geo-Resources, 2025;11(1):79.
7. Salman MM, Radhi NS, Sabr OH, Nhabih HT. Utilization of diverse cheap materials as pore generating agent to manufacture low-cost porous ceramic. Cerâmica, 2020;66:179–185.
8. Salman MM, Nhabih HT. Assessment of the partial and total replacement of feldspar by waste glass on porcelain properties. J. Ceram. Proc. Rese., 2020;21(3):371–377.
9. Hussein AM, Nhabih HT, Jabbar DN. Environmental impact of fuel stations on some heavy metal concentrations in nearby surface crust soils in urban areas: A case study of soil heavy metal contamination. IOP Conf. Series: Materials Science and Engineering, 2020;745:012164.
10. Yang Y, Shao Z, Wang Y. A discretized virtual internal bond method for dynamic fracture simulation

of layered rocks under various loading rates[J]. Engineering Fracture Mechanics, 2025,327:111466.

11. Yang S, Cao M, Yong R, et al. Experimental investigation on mechanical behaviors and shear fracture mechanisms of rough jointed sandstone under conventional triaxial compression[J]. International Journal of Rock Mechanics and Mining Sciences, 2025;194:106205.
12. Wang W, Zhao B, Zhao Y. Effects of bedding orientation and loading rate on fracture behaviors in coal: Analysis of experiments[J]. Theoretical and Applied Fracture Mechanics, 2025;139:105012.
13. Li X, Lok T, Zhao J. Dynamic characteristics of granite subjected to intermediate loading rate[J]. Rock Mechanics and Rock Engineering, 2005;38(1):21–39.
14. Hajiabdolmajid V, Kaiser P. Brittleness of rock and stability assessment in hard rock tunneling[J]. Tunnelling and Underground Space Technology, 2003;18(1):35–48.
15. Hokka M, Black J, Tkalich D, et al. Effects of strain rate and confining pressure on the compressive behavior of Kuru granite[J]. International Journal of Impact Engineering, 2016;91:183–193.
16. Mahmutoglu Y. The effects of strain rate and saturation on a micro-cracked marble[J]. Engineering Geology, 2006;82(3):137–144.
17. Zhuang J, Mu Z, Malkowski P, et al. The role of advance rate in mining-induced stress and microseismic behavior during longwall face advance[J]. Geomatics Natural Hazards & Risk, 2025;16(1):2515536.
18. Smith Z, Griffith W. Influence of preexisting damage on dynamic fragmentation behavior of sandstone[J]. Journal of Structural Geology, 2025;199:105493.
19. Bagde M, Petros V. Fatigue properties of intact sandstone samples subjected to dynamic uniaxial cyclical loading[J]. International Journal of Rock Mechanics and Mining Sciences, 2005;42(2):237–250.
20. Li Y, Huang D, Li X. Strain rate dependency of coarse crystal marble under uniaxial compression: Strength, deformation and strain energy[J]. Rock Mechanics and Rock Engineering, 2014;47(4):1153–1164.
21. XH L, QJ H, SY W, et al. Nonlinear mechanical properties of coal rock under quasi-static strain rate[J]. Journal of China Coal Society, 2109;44(5):1437–1445.
22. Li X, Gong F, Tao M, et al. Failure mechanism and coupled static-dynamic loading theory in deep hard rock mining: A review[J]. Journal of Rock Mechanics and Geotechnical Engineering, 2017;9(7):767–782.
23. Rouhani H, Farrokh E. Failure analysis of Nehbandan granite under various stress states and strain rates using a calibrated Riedel-Hiermaier-Thoma constitutive model[J]. Geomechanics and Geophysics for Geo-Energy and Geo-Resources, 2024;10(1):157.
24. Zhang H, Qi S, Bian H, et al. Fracture-induced variations in mechanical properties of silty mudstone under triaxial stress[J]. Environmental Earth Sciences, 2025;84(12):332.
25. Liu L, Ouyang J, Yang W, et al. Strain rate effects on characteristic stresses and dynamic strength criterion in granite under triaxial quasi-static compression[J]. Applied Sciences, 2025;15(11):6214.
26. Sun Y, Kwok C, Duan K. Rate effect of rocks: Insights from DEM modeling[J]. International Journal of Rock Mechanics and Mining Sciences, 2024;181:105857.
27. Walton G, Gaines S. Evaluation of stress path and load rate effects on rock strength using compression testing data for Stanstead Granite[J]. International Journal of Rock Mechanics and Mining Sciences, 2023;169:105455.
28. Liu X, Zhang S, Xie Y, et al. Three-dimensional heterogeneity of the pore and fracture development and acoustic emission response characteristics of coal rocks in the Yunnan Laochang Block[J]. Energies, 2024;17(5):1207.
29. Wang G, Song L, Wang Q, et al. Experimental study on the mechanical properties, acoustic emission characteristics, and permeability evolution of sandstone under triaxial hydromechanical coupling[J]. Energy Science & Engineering, 2022;10(12):4466–4480.
30. Wang G. Study on permeability evolution mechanism of rock fracture process based on acoustic emission moment tensor theory[D]. Xuzhou: China University of Mining and Technology, 2022.
31. Jalalian M, Bagherpour R, Khoshouei M. The use of acoustic emission technique in MWD for mine to mill approach as a smart tool for sustainable mining[J]. scientific reports, 2025;15(1):25383.
32. Manthei G, Plenkers K. Review on in situ acoustic emission monitoring in the context of structural health monitoring in mines[J]. Applied Sciences, 2018;8(9):1595.
33. Zhao F, Li Y, Ye Z, et al. Research on acoustic emission and electromagnetic emission characteristics of rock fragmentation at different loading rates[J]. Shock and Vibration, 2018;2018:4680879.
34. Heimisson E, Naderloo M, Chandra D, et al. Applying and validating Coulomb rate-and-state seismicity models in acoustic emission experiments[J]. Tectonophysics, 2025;895:230574.
35. Sun Y, Yu F, Lv J. Research on the characteristics of acoustic emission activities of granite and marble under different loading methods[J]. Lithosphere, 2023;2023(1):2773795.
36. Cao A, Jing G, Ding Y, et al. Mining-induced static and dynamic loading rate effect on rock damage and acoustic emission characteristic under uniaxial compression[J]. Safety Science, 2019;116:86–96.

37. XJ F, RZ Z. Influence of loading rate on macro and micro formation mechanism of acoustic emission events in sandstone and granite[J]. Safety in Coal Mines, 2021;52(5):47–53.
38. Liang Y, Kong F, Zou Q, et al. Effect of strain rate on mechanical response and failure characteristics of horizontal bedded coal under quasi-static loading[J]. Geomechanics and Geophysics for Geo-Energy and Geo-Resources, 2023;9(1):52.
39. Alneasan M, Behnia M, Alzo'Ubi A. Experimental observations on the effect of strain rate on rock tensile fracturing[J]. International Journal of Rock Mechanics and Mining Sciences, 2022;160:105256.
40. Melchiorre J, Bertetto A, Rosso M, et al. Acoustic emission and artificial intelligence procedure for crack source localization[J]. Sensors, 2023;23(2):693.
41. Song T, Zhou Y, Yu X. Three-dimensional acoustic emission source localization method for layered rock considering anisotropic P-wave velocity[J]. Bulletin of Engineering Geology and the Environment, 2024;83(5):185.
42. Pujol J, Herrmann R B. A student's guide to point sources in homogeneous media[J]. Seismological Society of America, 1990;61(3):209–220.
43. Knopoof L, Randall M J. The compensated linear-vector dipole: A possible mechanism for deep earthquakes[J]. Journal of Geophysical Research, 1970;57(26):4957–4963.
44. Gutenberg B, Richter CF. Frequency of earthquakes in California[J]. Bulletin of the Seismological Society of America, 1994;34(4):185–188.
45. Feignier B, Young R P. Moment tensor inversion of induced microseisnmic events: Evidence of non-shear failures in the -4 < M < -2 moment magnitude range[J]. Geophysical Research Letters, 1992;19(14):1503–1506.
46. Hudson J A, Pearce R G, Rogers R M. Source type plot for inversion of the moment tensor[J]. Journal of Geophysical Research: Solid Earth, 1989;94(B1):765–774.
47. Turcotte D L. Fractals in geology and geophysics[J]. Pure and Applied Geophysics, 1989;131:171–196.